

Figure 4.21: Effect of the density ratio on the trajectory of a wobbling bubble. Green bubble: density ratio = 10. Grey bubble: density ratio = 100. On the right: The straight line corresponds to ratio = 10.

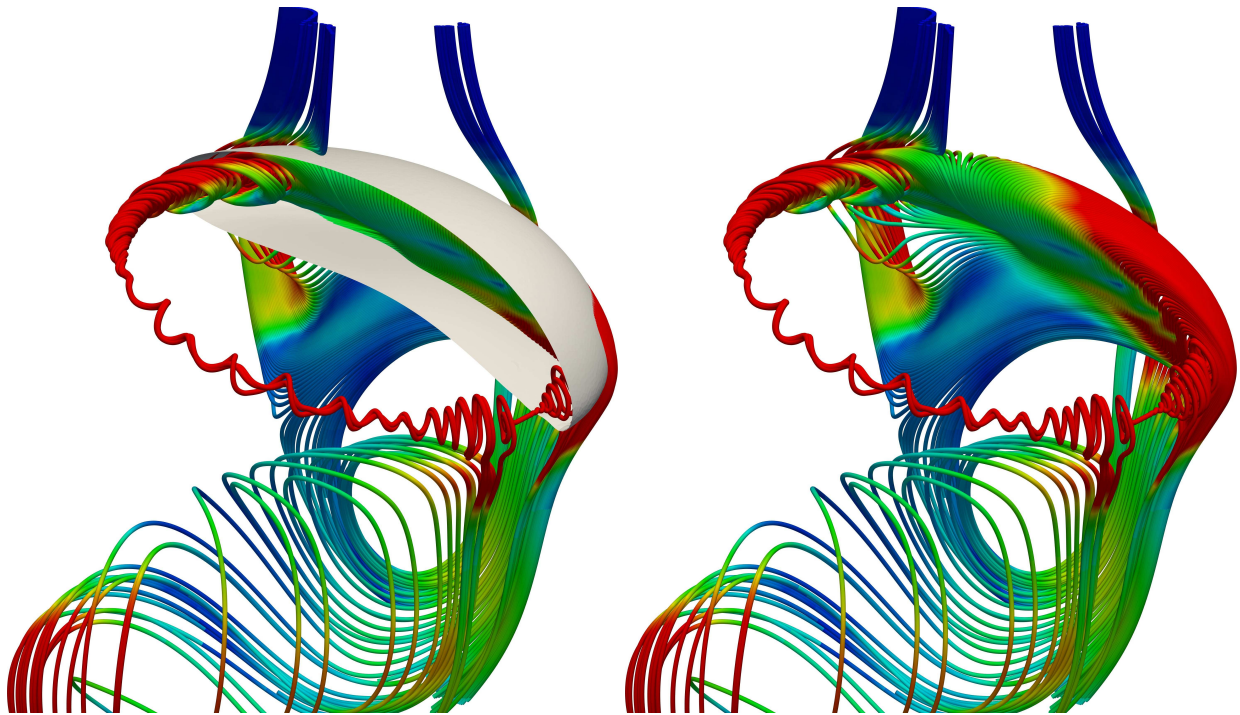


Figure 4.22: Streamlines showing a toroidal vortex inside the bubble and another vortex downstream. Density ratio $\lambda_\rho = 10$.

Sensitivity Analysis - Conclusions

This section has presented a sensitivity study in order to determine the influence of a set of simulation parameters on the outcome of the flow. Volume recovery and non-physical undulation



Figure 4.23: Patches of the finest level of the adaptive mesh. Refinement was performed based on the vorticity magnitude, as well as on the position of the Lagrangian interface.

removal algorithms have shown good results, by maintaining the bubble shape and conserving its volume.

When studying the influence of the Eulerian domain size on the bubble shape and Re number, a domain with 8ϕ between lateral boundaries has shown to be a commitment solution between computational cost and flow details.

Regarding domain resolution, an Eulerian grid spacing $h = \phi/32$ was chosen along with a Lagrangian mesh with mean edge length as small as half the Eulerian grid spacing at its finest level, since no significant gains were found with further refinement.

Therefore, further simulations will adopt the following configuration: Given a bubble with diameter ϕ , set to rise in the $+z$ -direction, the dimensions of the Eulerian domain will be $(8\phi \times 8\phi \times Lz)$, and the initial position of the bubble will be $(4\phi \times 4\phi \times 2\phi)$. The dimension Lz will

depend on the case being simulated, but a minimum length $L_z = 24\phi$ will be adopted. Since the ratio between the Eulerian grid spacing and the mean edge length in the Lagrangian mesh was set to $\lambda_\xi = 2$, the Lagrangian mean edge length will be set to $\xi_L = \phi/64$. In all cases, the volume recovery algorithm and the non-physical undulation removal will be used. Also, a density ratio $\lambda_\rho = 100$ will be adopted.

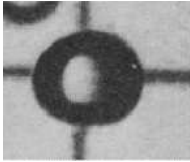


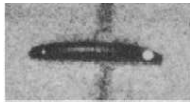


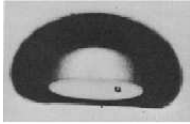
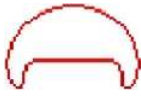

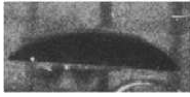



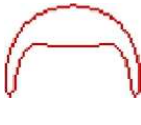




4.2.3 Terminal bubble shape and Reynolds number for low Reynolds flows

The ability of the current algorithm for predicting the terminal bubble shape and Reynolds number was tested against the experimental work of Bhaga and Weber (1981) for a series of low Re flows in different regimes. Also, two numerical works were used for comparison: Hua and Lou (2007) developed an axisymmetric algorithm with two volume-recovery steps for the Lagrangian interface per time step: after remeshing the interface and after the interface advection. Stene (2010) developed a 3D algorithm based on Berger's SAMR methodology for the discretization of the Eulerian domain. The Lagrangian framework, however, followed the approach of Hua and Lou (2007), requiring two volume-recovery steps per time step.

Table (4.10) shows various bubble regimes, ranging from low Re - low Eo spherical bubbles to moderate Re - moderate Eo skirted bubbles. A comparison with the experimental results shows that the present algorithm was able to predict the bubble shape properly. Regarding the terminal Re number, the maximum error occurred at the creeping flow regime, and so did the work of Hua and Lou (2007). Stene (2010) reports, for the same case, a relative error $\varepsilon = 21\%$ and suggests that the distance between the bubble and the domain boundaries could have influenced the results at this regime. However, in all cases in this work, the domain size was calculated based on the bubble initial diameter, as explained in section 4.2.2, and similar approach was also reported in (STENE, 2010).

In the remaining cases, the largest errors occurred for bubbles in the skirted regime, probably due to the decrease in the bubble thickness in the skirt regions. Possible remedies could be increasing the Eulerian grid resolution and/or the implementation of an algorithm for dealing with fragmentation mechanisms.

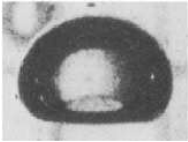


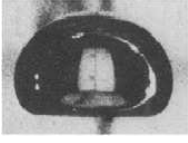
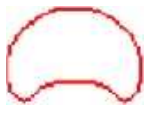


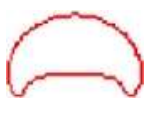




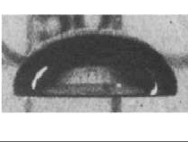
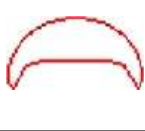


Table 4.10: Comparison of terminal shapes and Reynolds number reported by the reference works (BHAGA; WEBER, 1981; HUA; LOU, 2007) and the present work.

	Bhaga and Weber (1981)	Hua and Lou (2007)	Present Work
$E_o = 17.7$ $M=711$ $Re=0.232$		 $Re=0.211$ $\epsilon = 9.05\%$	 $Re=0.212$ $\epsilon = 8.62\%$
$E_o = 32.2$ $M=8.2e-4$ $Re=55.3$		 $Re = 52.96$ $\epsilon = 4.23\%$	 $Re = 53.2$ $\epsilon = 3.80\%$
$E_o = 243$ $M=266$ $Re=7.77$		 $Re = 8.40$ $\epsilon = 8.07\%$	 $Re = 7.61$ $\epsilon = 2.06\%$
$E_o = 115$ $M=4.63e-3$ $Re=94.0$		 $Re = 88.70$ $\epsilon = 5.64\%$	 $Re = 90.50$ $\epsilon = 3.73\%$
$E_o = 339$ $M=43.1$ $Re=18.3$		 $Re = 17.91$ $\epsilon = 2.13\%$	 $Re = 17.06$ $\epsilon = 6.78\%$
$E_o = 641$ $M=43.1$ $Re=30.3$		 $Re = 28.54$ $\epsilon = 1.22\%$	 $Re = 31.47$ $\epsilon = 5.81\%$

The influence of the Morton number on low Reynolds flows was also studied. Table (4.11) shows five cases of dimpled spherical cap bubbles at $E_o = 116$ and Morton number ranging from $M = 848$ to $M = 1.31$. As in the previous case, the results were checked against Bhaga and Weber (1981) and Hua and Lou (2007). The terminal bubble shape again was well predicted and the highest relative error on the prediction of the terminal Re number occurred for the case with the lowest terminal Reynolds.


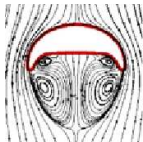
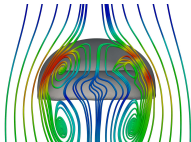

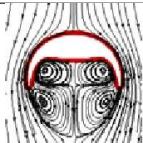
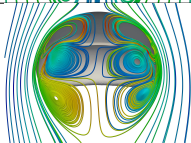
Regarding the flow pattern around the bubbles, Bhaga and Weber (1981) observed the existence of a closed toroidal wake through the flow visualization using hydrogen tracers, which appear as bright lines in the photographs shown in Table (4.12). Results obtained in the present work and also reported on Hua and Lou (2007) show a secondary wake recirculation just behind the bubble rim. This could be the reason for the bright spots observed in the lower outside part of

Table 4.11: Comparison of terminal shapes and Reynolds number reported by the reference works (BHAGA; WEBER, 1981; HUA; LOU, 2007) and the present work. Influence of the Morton number on the terminal shapes and Reynolds number.

	Bhaga and Weber (1981)	Hua and Lou (2007)	Present Work
Eo = 116 M=848 Re=2.47		 Re=2.317 $\varepsilon = 6.18\%$	 Re=2.34 $\varepsilon = 5.32\%$
Eo = 116 M=266 Re=3.57		 Re = 3.621 $\varepsilon = 1.45\%$	 Re = 3.67 $\varepsilon = 2.68\%$
Eo = 116 M=41.1 Re=7.16		 Re = 7.00 $\varepsilon = 2.19\%$	 Re = 6.97 $\varepsilon = 2.61\%$
Eo = 116 M=5.51 Re=13.3		 Re = 13.17 $\varepsilon = 0.99\%$	 Re = 12.89 $\varepsilon = 3.11\%$
Eo = 116 M=1.31 Re=20.4		 Re = 19.88 $\varepsilon = 2.56\%$	 Re = 19.64 $\varepsilon = 3.71\%$
Eo = 116 M= 8.6×10^{-4} Re=151			
		Re = 19.88 $\varepsilon = 2.56\%$	Re = 19.64 $\varepsilon = 3.71\%$ ver depois

the bubble rim in the first case. Notice that this recirculation becomes bigger in the second case, which explains the bright region in the photograph of the experimental case. Notice that, for this case, values for the terminal Reynolds numbers are not available in (HUA; LOU, 2007).

Table 4.12: Comparison of terminal bubble wake observed in experiments (BHAGA; WEBER, 1981) and predicted in simulation (HUA; LOU, 2007) for various Reynolds, Morton and Eotvos numbers against results obtained in the present work.

	Bhaga and Weber (1981)	Hua and Lou (2007)	Present Work
Eo = 116 M=0.962 Re=22.0			 Re=21.37 $\varepsilon = 2.85\%$
Eo = 292 M=26.7 Re=22.1			 Re = 17.48 $\varepsilon = 20.56\%$

Influence of the initial bubble shape

Studying the experimental setup designed by Bhaga and Weber (1981) shows that the device used for releasing the bubbles may have influence on the initial bubble shape. The complete apparatus is shown in Fig. (4.24). The bubble release mechanism is based on a dump cup (number 3) which temporarily holds the bubble and then releases it into an inverted funnel (number 5) through which the bubble (number 16) is then released for ascending through the test column (number 1). Since this mechanism may lead to different bubble shapes, a study was performed in order to assess the influence of the initial bubble shape on the outcome of the bubble flow (HUA; LOU, 2007).

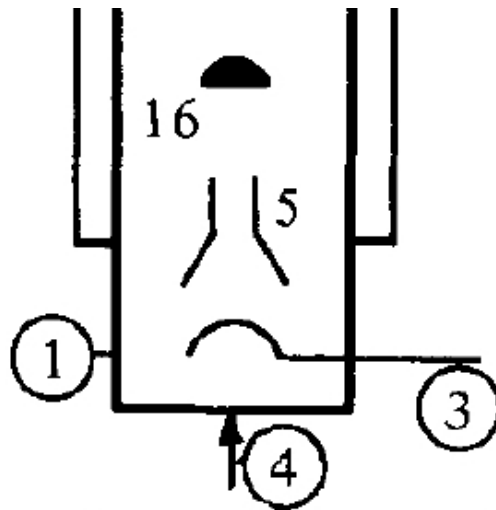


Figure 4.24: A simplified schematic drawing of the experimental apparatus utilized by Bhaga and Weber (1981), showing the bubble release mechanism: 1, test column; 3, dumping cup; 4, air inlet; 5, inverted funnel; 16, rising bubble.

The study was performed by simulating two cases with different initial shapes. In the first case, the study was performed based on the third case in Tab. (4.11), for which $EO = 116$, $M = 41.1$ and $Re = 7.16$. Three ellipsoidal bubbles with different aspect ratios but with the same volume were released, and the temporal evolution of their shape during the flow is shown in Fig. (4.25). The aspect ratio was defined as the height-to-width ratio, so that the bubble on the left has $\lambda_{H/L} = 0.59$, the bubble on the center has $\lambda_{H/L} = 1.0$ (therefore a sphere) and the bubble on the right has $\lambda_{H/L} = 1.31$. A comparison between this figure and Fig. (4.26) shows that the initial bubble with higher aspect ratio has higher initial rising velocity due to the lower drag force. As the bubbles approach the terminal shape, the terminal velocity converges to the same value in all cases.

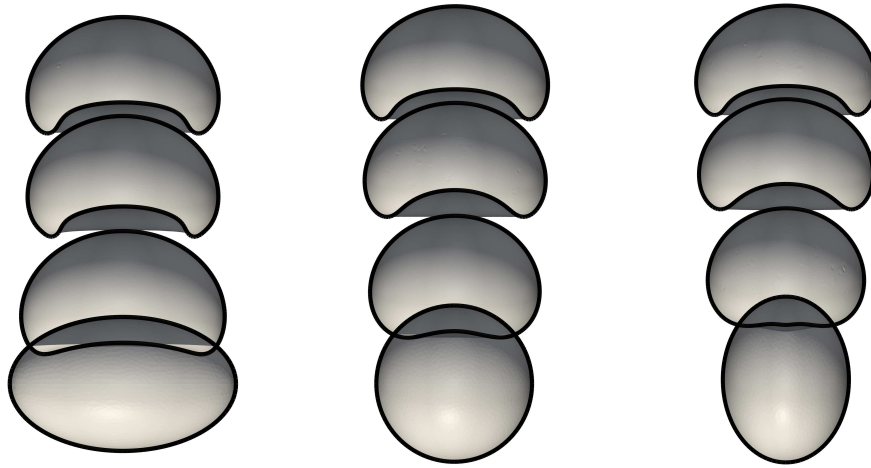


Figure 4.25: Influence of the initial shape on the evolution of the bubble shape. $Eo = 116$, $M = 41.1$, $Re = 7.16$.

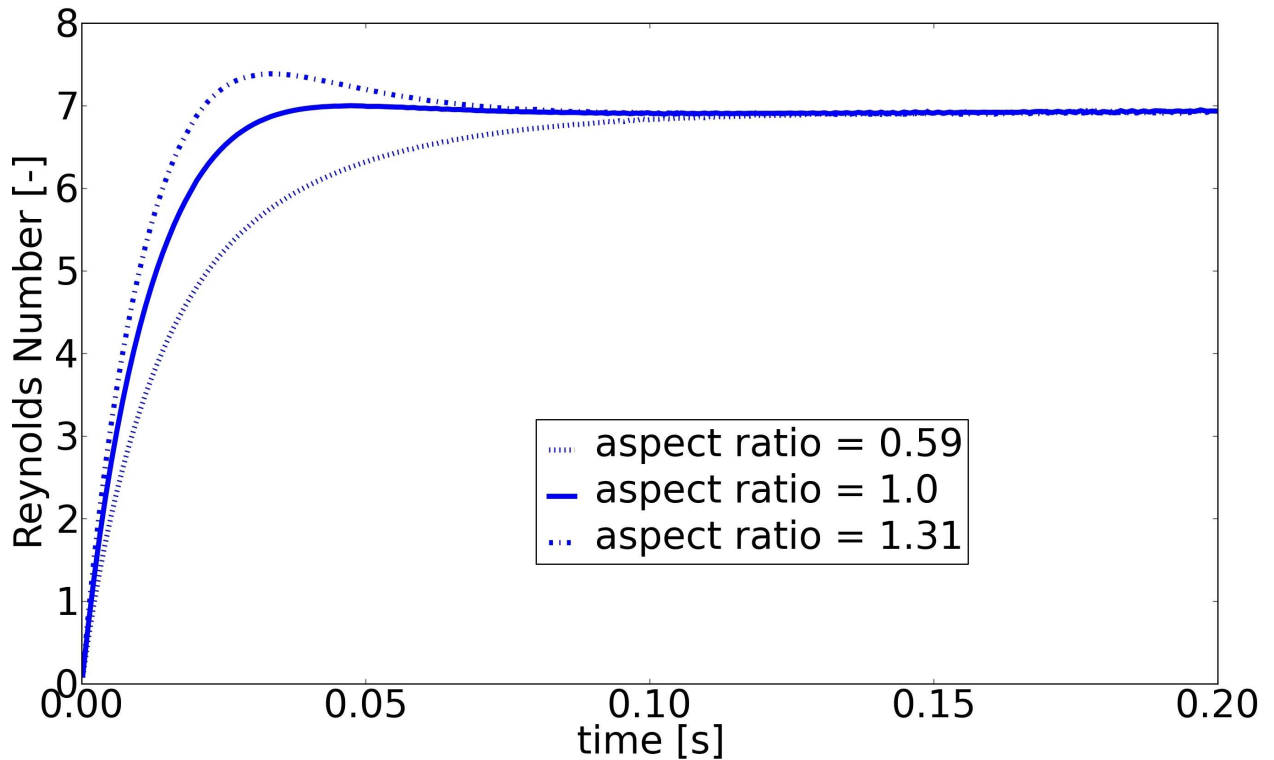


Figure 4.26: Influence of the initial shape on the Reynolds profile. $Eo = 116$, $M = 41.1$, $Re = 7.16$.

The second study was performed on a case with low Morton number ($Eo = 116$, $M = 8.6 \times 10^{-4}$ and $Re = 151$). Four different initial shapes were used for the bubble (the volume was kept constant): $\lambda_{H/L} = 0.59$, $\lambda_{H/L} = 0.85$, $\lambda_{H/L} = 1.0$ and $\lambda_{H/L} = 1.31$. As can be seen from Fig. (4.27), in this case the initial shape plays great influence on the evolution of the bubble shape. As the aspect ratio increases, the smaller drag force increases the ascending velocity, as can be seen from Fig. (4.28). These bubble will accelerates as long as the buoyancy force is greater than the drag force acting on the bubble. This leads to a high pressure gradient at the rear of the bubble,

which induces an upward liquid jet underneath the bubble. The drag force on the upper surface of the bubble is relatively steady, while the upward jet pushes the bottom of the bubble upwards, generating the dimpled shape. Therefore, the final bubble shape will depend on the relative strength of the upward liquid jet and the surface tension. If the jet is strong enough, the upper surface of the bubble is pierced by the jet, resulting in a toroidal bubble as seen in Fig. (4.27) for the bubbles with aspect ratio greater than 0.59.

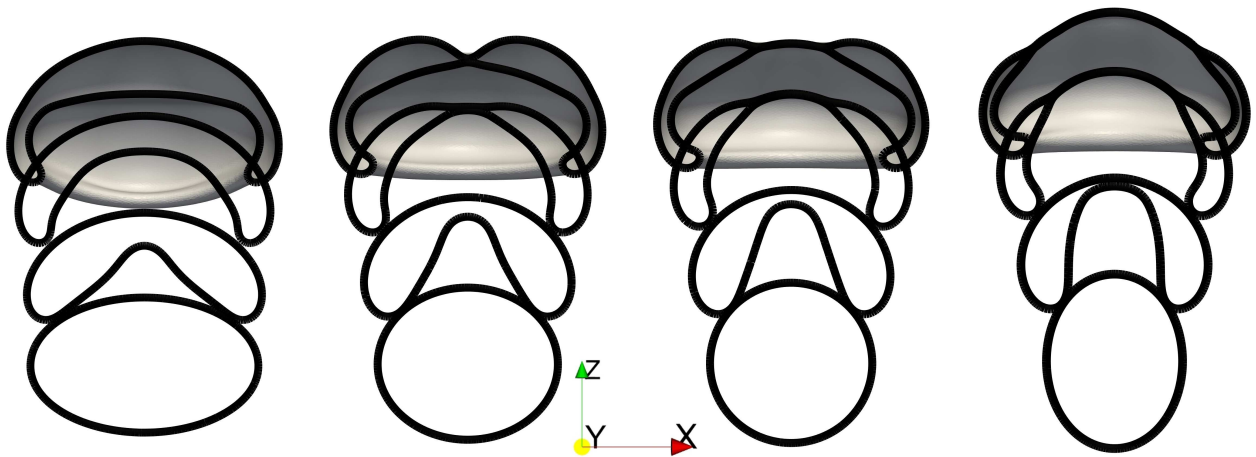


Figure 4.27: $Eo = 116$, $M = 8.6 \times 10^{-4}$, $Re = 151$. Influence of the initial shape on the evolution of the bubble shape.

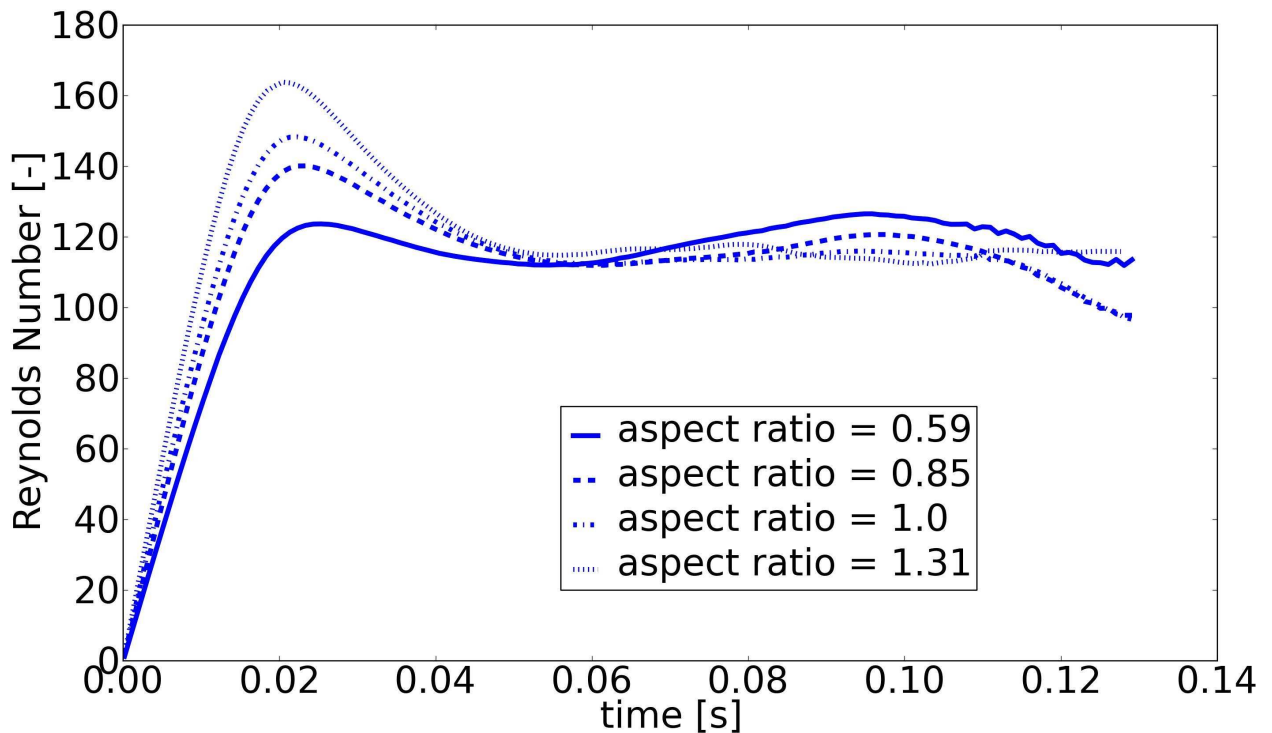


Figure 4.28: $Eo = 116$, $M = 8.6 \times 10^{-4}$, $Re = 151$. Influence of the initial shape on the Reynolds number profile.

4.2.4 Wobbling

Two cases were simulated in order to assess the ability of the algorithm for dealing with bubbles rising in an oscillating path. In the first case, the bubble was characterized by $Eo = 10$ and $M = 9.78 \times 10^{-8}$ and, from the Clift diagram (CLIFT; GRACE; WEBER, 1978), $Re \approx 280$. The following physical parameters were used: $\phi = 0.0034m$, $\sigma = 0.01N/m$, $\rho_C = 1000kg/m^3$, $\mu_C = 0.0018Pa \cdot s$ and $g = 9.81m/s^2$ in the $-z$ -direction. Density and viscosity ratios were set to 100. The Eulerian domain was set to $(8\phi \times 8\phi \times 80\phi)m$ and six levels of refinement were used.

According to Stene (2010), such bubble should rise following a zigzag path, which is characterized by a predominantly two-dimensional oscillating movement. Figure (4.29), which shows the centroid path during the simulation, shows that although this happens at the initial stages of the flow, a transition to a spiral path takes place, and the bubble reaches the steady state following this movement.

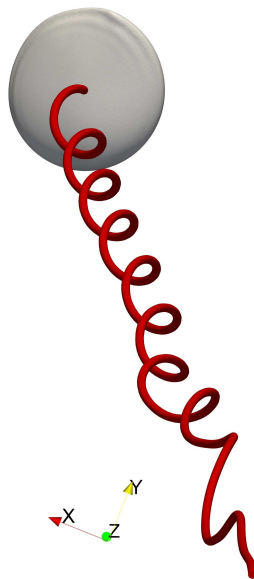


Figure 4.29: Wobbling bubble, $Eo = 10$ and $M = 9.78 \times 10^{-8}$. Centroid path shown in 3D. The zigzag path can be seen in the beginning of the flow, and then the transition to spiral .

This effect is clearly seen in Fig. (4.30), which shows the time history of the velocity profile of the bubble centroid. In the beginning of the simulation, when $t < 0.2s$, the plot clearly shows a zigzag path in the yz -plane, since the velocity magnitude is much smaller in the x -direction. However, as time evolves, this velocity component increases and, after $t = 0.4s$, x - and y - components reach a comparable magnitude. Simultaneously, the z -component of the velocity converges to an

asymptotically constant value.

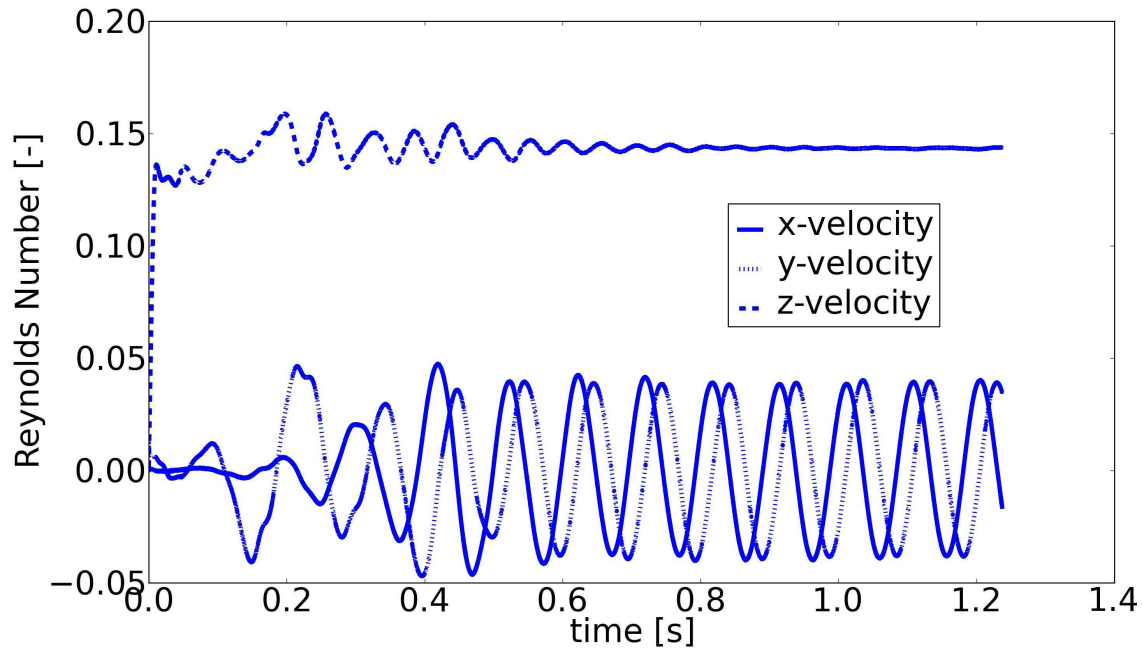


Figure 4.30: Wobbling bubble, $Eo = 10$ and $M = 9.78 \times 10^{-8}$. Velocity profile of the bubble centroid.

The bubble wake is illustrated by the Q-criterion, and an iso-value $Q = 5000$ is shown in Fig. (4.31). Hairpin unstable eddies can be seen downstream of the bubble, which rises in the z-direction. These eddies, which are responsible for the transition to turbulence, are similar to those found in flows over a rigid sphere.

An example of the adaptive refinement can be seen in Fig. (4.32), which shows a planar slice of the grid showing the fine grid around the high vorticity regions (the shaded regions in the picture).

Figure (4.33) shows the flow inside the bubble. The velocity field is shown by plane slices which are warped according to the velocity vector. Also, the velocity vectors located at these slices are shown. The slices are coloured by the density field. The velocity vectors are coloured by the velocity magnitude.

The next case simulated was based on Gaudlitz and Adams (2009), who simulated an air bubble rising in quiescent water. The density ratio used in the paper was $\lambda_\rho = 774$ and the viscosity ratio employed was $\lambda_\mu = 54$. Here, the same viscosity ratio was used, but the density ratio was